Completion of a Truncated Attenuation Image from the Attenuated PET Emission Data

Johan Nuyts[1], Girish Bal[2], Frank Kehren[2], Matthias Fenchel[3], Christian Michel[2], Charles Watson[2]

***Abstract*—Positron emission tomographs (PET) are currently almost exclusively designed as hybrid systems. The current standard is the PET/CT combination, while prototype PET/MRI systems are being studied by several research groups. One problem in these systems is that the transaxial field of view of the second system is smaller than that of the PET camera and does not provide complete attenuation data. Because this second system provides the image for PET attenuation and scatter correction, the smaller field of view causes truncation of the attenuation map, producing bias in the attenuation corrected activity image. In this paper, we propose a maximum-a-posteriori algorithm for estimating the missing part of the attenuation map from the PET emission data. The method is evaluated on five artificially truncated ^{18}F-FDG PET/CT studies, where it reduced the error on the reconstructed PET activities from 20% to less than 7%. The results on a PET/MRI patient study with ^{18}F-FDG are presented as well.**

I. INTRODUCTION

In hybrid PET systems, there are two hurdles complicating the estimation of the PET attenuation map. One is the truncation of the attenuation map due to the small field of view of the MRI or CT system, the other one is the conversion of the image values to linear attenuation coefficients at 511 keV. Although not fully solved for PET/CT systems, the current conversion methods produce satisfactory results in most cases [1]. The problem is more difficult in MRI, because the MRI signal does not correlate with the linear attenuation coefficient. In this paper, the conversion problem is not considered; it is simply assumed that an effective method is available for transforming the possibly truncated MRI image into the corresponding truncated PET attenuation image [2]. An overview of existing methods is given in [3]. We also assume that the deformation of the MR image inside the field-of-view is negligible.

In CT, the truncation problem can be mitigated by data extrapolation techniques [4], [5] or by iterative reconstruction [6]. In MRI, truncation correction can be more difficult. In this paper, a method is proposed to estimate the truncated attenuation from the PET emission data. This problem is a milder version of the problem of simultaneously estimating the entire attenuation map (and the tracer distribution) from the attenuated emission data. The latter problem has been studied by several groups, both for PET and SPECT [7]–[15]. Different types of consistency conditions can be considered. The analytical consistency conditions include integral expressions (Helgason-Ludwig conditions [8], [9], [16]) and local consistency conditions [17]. Discrete consistency conditions have been used in [11], [14], [18]. Consistency can also be imposed by maximizing the likelihood function [10], [13], [19]. Here, we present results on an adaptation of the iterative "MLAA" reconstruction algorithm of [10] to the problem at hand (MLAA stands for maximum likelihood reconstruction of attenuation and activity).

Recently, Salomon et al. proposed a related maximum-likelihood (ML) algorithm, not for estimating the truncated region but for assigning attenuation values to MRI-regions, based on time-of-flight PET data [20]. Laymon et al. used an ML-approach to recover localized defects in the (non-TOF) PET attenuation map in small pre-defined regions, assuming that the rest of the attenuation map was known [19], [21]. This problem is similar to the truncation problem studied here. The main difference is that in [21], the updated regions are small and located well inside the field-of-view, and the algorithm was constrained to assign only one of two predefined attenuation coefficients (bone or soft tissue).

In the following, the proposed (modified) MLAA algorithm is described. The sensitivity to some of the parameters is illustrated on simple 2D simulations. The algorithm has been evaluated using five PET/CT patient data sets, where the (nearly) untruncated CT-image was truncated to a reduced field-of-view. The truncated part of the CT-based attenuation map was estimated with MLAA, and the results were compared to those obtained with the original, untruncated attenuation map. We also examined the sensitivity of the MLAA-approach to segmentation errors in the known part of the attenuation map, and to scatter correction. A simulation experiment was done to assess the performance of the MLAA algorithm for reconstructing cold objects, such as coils, which are generally not included in the measured, truncated attenuation map. Finally, the result obtained on a patient scan from the Siemens hybrid PET/MRI system is presented.

II. METHODS

A. Objective function

Let $y_i, i = 1 \dots I$ represent the measured (attenuated) PET data acquired by detector pair i. The expectation $\bar{y}_i$ of the data y_i can be written as

$$\bar{y}_i = \sum_j g_{ij} a_i \lambda_j + s_i \quad \text{and} \quad a_i = \exp(-\sum_j l_{ij} \mu_j) \qquad (1)$$

where λ_j is the amount of radioactivity in j, g_{ij} is the probability that a unit activity in j contributes a detection event

---

[1] Nuclear Medicine, K.U.Leuven, B-3000 Leuven, Belgium, [2] Siemens Medical Solutions, MI, Knoxville, TN, USA, [3] Siemens AG, Erlangen, Germany.

to line of response (LOR) i in absence of attenuation, a_i is the probability that a photon pair travelling along LOR i will not be lost due to attenuation, l_{ij} is the intersection length of LOR i with voxel j, μ_j is the linear attenuation coefficient in voxel j and s_i is an estimate of the scatter (and possibly random) contributions.

We assume that reliable estimates of μ_j are available for the central part of the PET field of view. Outside that region, however, μ_j is unknown. Denoting the region where μ is known as K and its complement as U, we can write

$$a_i = m_i \exp(-\sum_{j \in U} l_{ij}\mu_j) \text{ with } m_i = \exp(-\sum_{j \in K} l_{ij}\mu_j) \tag{2}$$

The PET data are acquired to produce the image $\hat{\lambda}$, which is an estimate of the true tracer distribution λ. To reconstruct this image from the data y, we have to estimate the unknown attenuation values $\{\mu_j, j \in U\}$ as well. Because raw PET data are Poisson distributed, the log-likelihood of this estimation problem can be written as

$$\begin{aligned} L(\hat{\lambda}, \hat{\mu}; y, m) &= \sum_i y_i \ln(\hat{y}_i) - \hat{y}_i && (3) \\ \hat{y}_i &= \sum_j g_{ij} \hat{a}_i \hat{\lambda}_j + s_i && (4) \\ \hat{a}_i &= m_i \exp(-\sum_{j \in U} l_{ij}\hat{\mu}_j) && (5) \end{aligned}$$

This function is maximised to estimate $\hat{\mu}$ and $\hat{\lambda}$. Because this problem is under-determined, regularisation is recommended. To encourage smooth solutions of $\hat{\mu}$, two priors are combined for the attenuation image. The first prior $P_1(\hat{\mu})$ favours the attenuation coefficients of air and tissue. It is assumed that the truncated part will contain mostly air, tissue and bone, the lungs should be in the region K. The prior is created by combining Gaussian functions centered at the favoured attenuation values [10]. This prior has obviously local maxima, and more so when the number of favoured attenuation values increases. For that reason only modes for air and tissue were used. The second prior $P_2(\hat{\mu})$ is the relative difference prior of [22]. This Markov prior is similar to the quadratic prior, except that it penalises relative differences between neighbouring pixels rather than absolute differences. In addition, it has a parameter (called γ in [22]) which optionally introduces increased tolerance of the prior to large relative differences.

The reconstruction of the activity image is also regularised with the relative difference prior. Because its parameters may be different from the parameters used in $P_2(\hat{\mu})$, we denote it with a different symbol $P_3(\hat{\lambda})$. Thus, the objective function L of (3) is replaced with the posterior function Q:

$$\begin{aligned} Q(\hat{\lambda}, \hat{\mu}; y, m) &= L(\hat{\lambda}, \hat{\mu}; y, m) && (6) \\ &+ \beta_\mu \left(P_1(\hat{\mu}) + \beta_2 P_2(\hat{\mu})\right) + \beta_\lambda P_3(\hat{\lambda}), \end{aligned}$$

where β_μ and β_λ determine the strength of the priors, while β_2 is used to balance the relative strengths of the two priors for the attenuation coefficients.

B. Optimisation

The reconstruction of the activity $\hat{\lambda}$ and of the missing attenuation $\hat{\mu}$ is obtained by maximising Q. As in [10], this is done by alternated maximisation. First, Q is increased by updating $\hat{\lambda}$, keeping $\hat{\mu}$ at its current value. Then, Q is further increased by updating $\hat{\mu}$. This sequence is considered a single iteration, and it is repeated until convergence is deemed satisfactory.

With fixed $\hat{\mu}$, the optimisation of Q reduces to standard maximum-a-posteriori (MAP) reconstruction in emission tomography. Hence, an update of $\hat{\lambda}$ is computed with a single iteration of a MAP-algorithm, here we used the algorithm proposed in [22]. In this step, the priors P_1 and P_2 can be ignored because they are independent of λ.

Combining (4) and (5) one obtains:

$$\hat{y}_i = (\sum_j g_{ij}\hat{\lambda}_j m_i) \exp(-\sum_{j \in U} l_{ij}\hat{\mu}_j). \tag{7}$$

Consequently, with fixed $\hat{\lambda}$, the optimisation of Q reduces to standard MAP reconstruction in transmission tomography. The first factor in (7) represents all the activity along LOR i, weighted with the detection probabilities g_{ij} and attenuated by the known attenuation in K. This quantity plays the role of the blank scan in standard transmission tomography. For the update of $\hat{\mu}$, we used a MAP reconstruction for transmission tomography [10], [23] with the priors P_1 and P_2.

The reconstruction was accelerated by using ordered subsets [24]. It was found that interleaving the emission and activity updates was more effective when done within each subset. Thus, for each subset, first $\hat{\lambda}$ is updated and then $\hat{\mu}$. We used 6 iterations with 42 subsets.

Details about the algorithm are given in the appendix.

C. Parameter values

The parameter γ was set to 5 in $P_1(\hat{\mu})$ and $P_2(\hat{\mu})$ and to 20 in $P_3(\hat{\lambda})$ based on visual inspection of the resulting images. We found that the results are less sensitive to β_λ than to β_μ, but the same set of parameters produced good results in all patients, suggesting that the method is robust enough and can be applied in clinical practice.

D. The "clinical" reconstruction

The MLAA algorithm estimates both the attenuation and the activity, but the appearance of the activity image is different from typical clinical OSEM (ordered subsets expectation-maximisation [24]) images, because of the high number of iterations and the use of $P_3(\hat{\lambda})$. Therefore, a final "clinical" activity image is computed with OSEM using the MLAA-estimated attenuation map.

III. EXPERIMENTS

This section gives a brief overview of the experiments carried out to evaluate the MLAA algorithm, the results are presented in the same order in the next section.

A. Simulations assessing the influence of the prior weights

A set of 2D simulations was done for a simplified slice through the thorax. It has four different attenuation coefficients (air, lung, tissue, bone) and four levels of activity (air, lung, tissue, heart). An image is shown in figure 1. The value of

β_2 in (6) was determined with trial and error, and then the values of β_μ and β_λ were varied over two orders of magnitude (in 8 steps), to illustrate how they affect the pixel bias and pixel variance of the final "clinical" OSEM reconstruction. For each pair $(\beta_\mu, \beta_\lambda)$, 50 noise realisations have been computed. Sinograms of 80 LORs × 96 angles were used with a total of 436000 counts. This study was only done to assess the effect of the prior weights on the behaviour of the algorithm. For the 3D studies, a different pair of values β_μ and β_λ was selected based on visual inspection.

B. *Truncated CT-based attenuation maps*

The method was evaluated in five ^{18}F-FDG whole body patient data sets from two PET/CT systems (Siemens Biograph16 for studies 1-4 and Biograph40 for study 5) having minimal or no truncation. In studies 1-4, the dosage was 192 - 350 MBq, depending on the weight, and the scan time was 3 min per bed position. For study 5, the dosage was 518 MBq and the scan time was 2 min per bed position.

The CT data (50 cm field of view (FOV)) were truncated to a central field of view of 40 cm (32 cm for study 5), and the algorithm was applied to estimate the missing attenuation values. It was assumed that the shape, position and attenuation of the patient table and head holder were known, and therefore, the table and head holder were also inserted as a known portion into the truncated image. Unless otherwise stated, the scatter estimate s_i in (4) was computed from the untruncated attenuation map using [25]. Correction for randoms was done with the standard real time pre-correction based on the delayed window technique.

"Clinical" emission images were reconstructed using 1) the untruncated attenuation map (reference), 2) the truncated attenuation map and 3) the truncated and MLAA based completed attenuation map. These images were compared to assess the severity of truncation induced errors, and the performance of the proposed completion algorithm. The "clinical" emission images were reconstructed with 3 OSEM iterations: one iteration of 21 subsets, followed by one with 16 and one with 8 subsets. This is roughly equivalent to 45 MLEM iterations, and of the same order as what is used in clinical protocols. The number of subsets is gradually decreased to reduce the suboptimal noise propagation due to convergence to a limit cycle [26].

C. *Completion of a segmented attenuation map*

As mentioned above, converting the MRI-voxel values to linear attenuation coefficients at 511 keV is a non-trivial problem. In particular the identification of bone is problematic. Some currently available segmentation methods produce approximate attenuation maps, where bone and soft tissue are combined in a single tissue class, which is set to the attenuation coefficient of soft tissue [2]. To simulate this approach, the CT-attenuation maps were segmented in a similar fashion (assigning a single attenuation coefficient to bone and soft tissues), and the performance of MLAA for estimating truncated parts was assessed as before.

D. *Influence of scatter correction*

In the experiments with patient data presented above, an estimate of the scatter contribution was created with the scatter correction algorithm of [25], using the original, non-truncated attenuation map. In practice, this extended FOV attenuation map will not be available, and some other, probably less accurate first estimate for the scatter contribution will have to be used. As shown by Laymon et al [27], failure to correct for scatter may well affect the performance of the estimation method. To evaluate the sensitivity of the MLAA performance to the scatter estimate, the MLAA algorithm has been applied to the patient studies without scatter correction (i.e. s_i in eq. (4) was set to zero). Finally, for one of the patient studies, the scatter estimates based on the untruncated CT and on the attenuation map estimated by MLAA were compared.

E. *MLAA-reconstruction of cold objects*

In the previous experiments, it was assumed that there was activity in the truncated parts of the attenuation map, as is the case for ^{18}F-FDG, which has a non-specific accumulation in the entire body. Therefore, these experiments will not predict the performance of MLAA for estimating the attenuation by cold objects that might be in the scanner but are not seen in the (truncated) anatomical image. In particular, in PET-MRI systems, body coils may be present in the PET-field of view, and these coils are not seen in the MRI-image.

As a first assessment of MLAA performance for reconstructing the attenuation of such cold objects, a simulation has been carried out. The NCAT phantom [28] was used to create a voxel model of the attenuation and activity images for a PET ^{18}F-FDG study. In front of the patient, 6 rods were placed. Three rods had a diameter of 10 mm and attenuation values of 0.2, 0.15 and 0.095/cm (i.e. higher than or equal to tissue). The other three rods had a diameter of 6 mm and attenuation coefficients of 0.095, 0.08 and 0.06/cm (i.e. less than or equal to tissue). A fully 3D PET acquisition using the Siemens TruePoint PET system geometry was simulated using analytical projection with attenuation. A noise-free scatter distribution was added. The resulting maximum count in the noise-free sinogram was 15, the total sinogram count was 67×10^6. Poisson noise was added using the noise-free sinogram as the mean of the Poisson distribution. MLAA reconstructions were made, allowing MLAA to modify the (initially zero) values of the attenuation near the rods.

F. *First results for a hybrid PET/MRI system*

Clinical data from the Siemens Biograph mMR scanner were used for the evaluation. Depending on the MR sequence used, the MR field of view could be about 50 cm in the transaxial plane [1]. Since the PET FOV is about 60 cm the above mentioned MLAA algorithm was used to estimate the truncated part of the attenuation map.

A list-mode scan (five bed positions) of a large patient in the supine position was acquired using the MR-PET system.

---

[1] Because the trusted FOV of the MR is ellipsoidal, its transaxial diameter depends on the axial position. The maximum diameter is approximately 50 cm.

The patient was injected with 329 MBq of ^{18}F-FDG and the MR-PET scan was performed 3 hours post injection. The scan was acquired for 11 minutes per bed position to compensate for the long post injection delay. The PET emission images were acquired simultaneously with the various MR sequences used to generate the MR based attenuation maps along with other MR images.

Randoms correction with variance reduction was applied [29]. The measured 344x252x837 projection data was down sampled to 172x126x837 to reduce reconstruction time. The truncated MR attenuation map (field-of-view was 50 cm), hardware attenuation map, normalization and the projection data were read in and the truncated part was estimated using the MLAA joint estimation algorithm. Twenty MLAA iterations with 9 subsets per iteration where used, ignoring the scatter contribution ($s_i = 0$ in eq. (4)). The PET emission images were reconstructed using the truncated as well as the MLAA based extended attenuation map using 3 OSEM iterations and 21 subsets.

IV. RESULTS

A. Simulations assessing the importance of the prior weights

Fig 1 shows the true attenuation and activity images, the known part of the attenuation, the MLAA completed attenuation image and the corresponding "clinical" reconstruction. Also the "clinical" reconstruction using the exact attenuation is shown for reference. Figure 2 shows the bias (root mean square of the pixel bias) and the average pixel standard deviation in the clinical activity image, while either β_μ or β_λ were varied above and below the optimal value (two orders of magnitude). With very low β_μ and β_λ, there is non-zero attenuation in the background and cross-talk between attenuation and activity near the boundaries. With strong β_μ but low β_λ, the attenuation map becomes too smooth, because image detail can be sent to the activity image via the cross-talk. Increasing β_λ reduces this effect. Finally, very high values of β_μ and β_λ result in increased bias due to over-smoothing. These effects are illustrated by images from the simulation shown in fig 3. These images are the mean over the 50 noise realisations for selected pairs of β_λ and β_μ. The central images correspond to the optimal values for beta (normalized to 1 in fig 2).

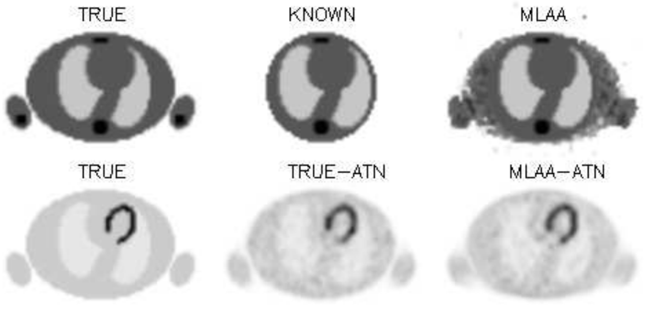

Fig. 1. An example from the 2D simulation. The first row shows the true attenuation (TRUE), the known part of the attenuation image and the MLAA completed attenuation image. The second row shows the true activity image (TRUE), and the "clinical" reconstructions based on the true attenuation (TRUE-ATN) and the MLAA-based attenuation (MLAA-ATN).

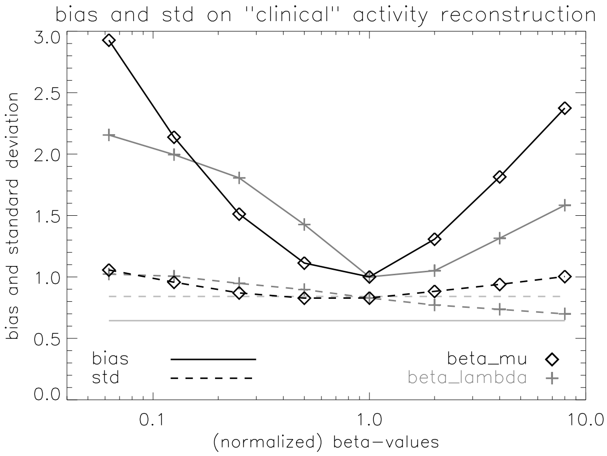

Fig. 2. The evolution of the average absolute value of the pixel bias and $\sqrt{\text{pixel variance}}$ as a function of β_μ and β_λ, while both regularisation parameters are changed around their optimal value (normalised to 1). The horizontal lines represent the average bias (solid) and standard deviation (dashed) of the reference "clinical" OSEM image. For comparison: the activities in heart, tissue and lungs are 64, 12.8 and 6.4 respectively.

B. Truncated CT-based attenuation maps

Figure 4 compares the MLAA-reconstructed activity image and the corresponding "clinical" OSEM reconstruction. The MLAA activity image produced with the prior $\beta_\lambda P_3(\hat{\lambda})$ of (6) is too smooth for clinical use.

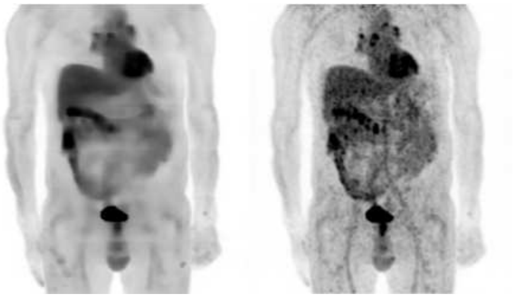

Fig. 4. Maximum intensity projections of the MLAA-reconstructed activity (left) and the corresponding "clinical" OSEM reconstruction (right, same color scale), for patient study p4.

Figure 5 shows maximum intensity projections of the three image sets (reference, truncated and MLAA-completed attenuation images) and their difference with the reference, for one particular patient. Figure 6 shows the corresponding results for the four other patients. The difference images reveal that activity values in the entire 3D PET image are affected (local and distant effects), although the local effects are stronger. The errors in hotter regions tend to be higher than in cold regions.

Regions of interest were drawn inside the arms in the attenuation image estimated by MLAA, to obtain the typical attenuation values produced by the algorithm. For comparison, the typical CT-based attenuation value was obtained in a similar way. The results are shown in Table I. MLAA typically underestimates the attenuation by about 13%.

Volumes of interest (VOI) were defined in the clinical OSEM images to assess the effect of truncation and MLAA-completion of the attenuation map on the reconstructed SUV-values. A large VOI was defined containing the truncated right

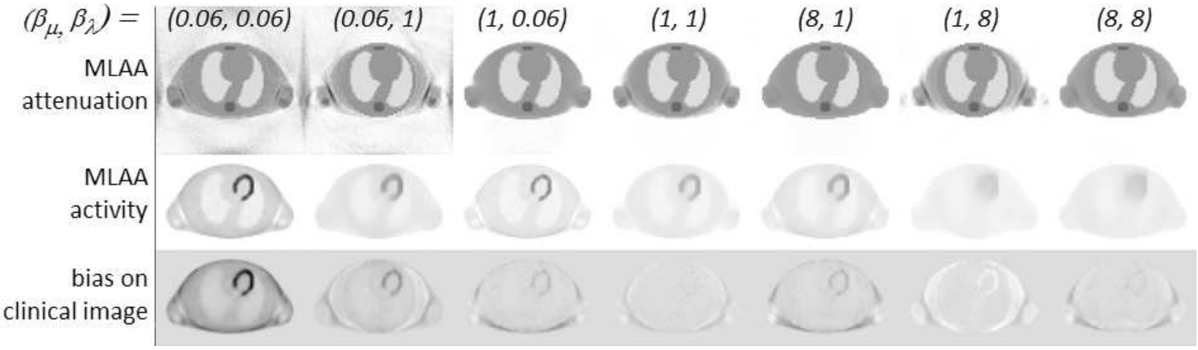

Fig. 3. MLAA reconstruction of the attenuation (row 1) and the activity (row 2), and the bias on the corresponding clinical images (row 3), for different combinations of beta. The values of β_μ and β_λ where set to 0.0625, 1 and 8, i.e. very low, optimal and very high (see fig 2). The results are shown for a different $(\beta_\mu, \beta_\lambda)$ pair in each column, as indicated in the figure. The images in the same row are shown with the same intensity scale, a different scale is used for each row.

TABLE I
ATTENUATION COEFFICIENTS ESTIMATED IN THE ARMS IN THE FIVE PATIENT IMAGES P1 . . . P5, AND THE CT-BASED ATTENUATION VALUE.

	P1	P2	P3	P4	P5	CT
mean [/cm]	0.087	0.087	0.085	0.087	0.091	0.10
std [/cm]	0.005	0.004	0.006	0.007	0.007	0.009

arm to evaluate the local effects. Additional VOIs were defined in structures with increased tracer uptake in the patient's body. The mean values and the standard deviations in these regions are listed in Table II. The location of some VOIs of patients 2 and 3 have been indicated in figure 6.

TABLE II
THE MEAN RECONSTRUCTED ACTIVITY (SUV) IN VOLUMES OF INTEREST IN REFERENCE ACTIVITY IMAGE (REF), THE IMAGE BASED ON TRUNCATED ATTENUATION (TRUNC), AND THE IMAGE BASED ON MLAA COMPLETED-ATTENUATION (MLAA)

		ref		trunc		mlaa	
		mean	*std*	mean	*std*	mean	*std*
p1	arm	0.91	*0.41*	0.099	*0.034*	0.45	*0.18*
	liver	2.95	*0.45*	2.39	*0.31*	2.76	*0.37*
p2	arm	0.50	*0.16*	0.24	*0.10*	0.37	*0.11*
	hand	4.6	*3.0*	3.1	*1.9*	4.2	*2.8*
	lung tumor	8.80	*2.3*	7.75	*2.0*	8.68	*2.2*
p3	arm	0.57	*0.3*	0.26	*0.16*	0.46	*0.24*
	rib (near liver)	2.86	*0.42*	2.23	*0.33*	2.68	*0.39*
	bowel	5.22	*1.0*	4.26	*0.8*	4.86	*1.0*
p4	arm	0.57	*0.25*	0.16	*0.09*	0.45	*0.18*
	mediast. lymph node	3.70	*0.63*	2.87	*0.47*	3.63	*0.61*
	bladder	23.4	*8.5*	20.0	*7.2*	22.5	*8.5*
p5	arm	0.76	*0.26*	0.16	*0.09*	0.65	*0.19*
	liver	2.63	*0.28*	2.05	*0.27*	2.58	*0.25*
	kidney	13.3	*11*	10.9	*9*	12.7	*11*

Figure 7 gives the relative errors on the reconstructed PET voxel values as a function of the reference standardised uptake value (SUV), computed from the five patient studies. For each patient, all voxels in the patient body were included. However, the image of the head of patient 5 (last column of fig 6) was excluded, because MLAA reconstructed a ring of additional attenuating material around the head holder. This yielded an increase of about 5% (range of 0-10%) of the high SUV-values in the brain. Because this effect was persistent and only occurred for the head holder of the Biograph40, we suspect MLAA may have attempted to correct small errors in the conversion from Hounsfield units to PET attenuation values for this particular head holder.

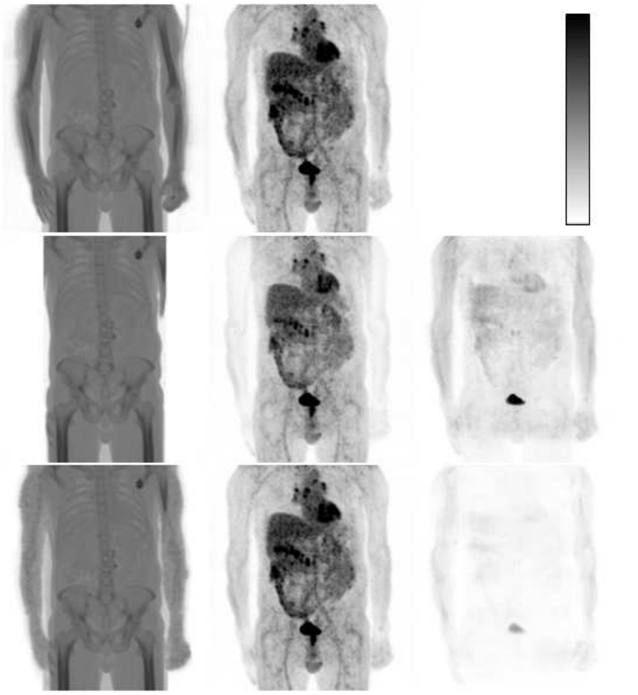

Fig. 5. The first row shows maximum intensity projections (MIP) of the CT-based attenuation (left) and the PET activity images (patient study p4). The second row shows the corresponding images in the case of truncation, the third image is the MIP of the difference image with the reference activity (absolute value of pixel differences). The third row shows the completed attenuation image (left), the MIP of the PET activity (center) and the MIP of the difference with the reference activity (right). All reconstructions were done with a scatter estimate from the untruncated attenuation map.

The truncation of the arms causes the SUV to be underestimated by about 20%. After MLAA-based estimation of the missing attenuation values, this error was reduced to about 6% or less. Also the spread around the mean value was strongly reduced. Note that the reference is a good but imperfect approximation of the ground truth. E.g., in one of the patients there was a truncation artifact in the CT as well (p1 in fig 6).

C. Completion of a segmented attenuation map

When the bone was segmented away in the known attenuation, the performance of MLAA was similar as for the non-segmented attenuation maps. Figure 8 shows the results for

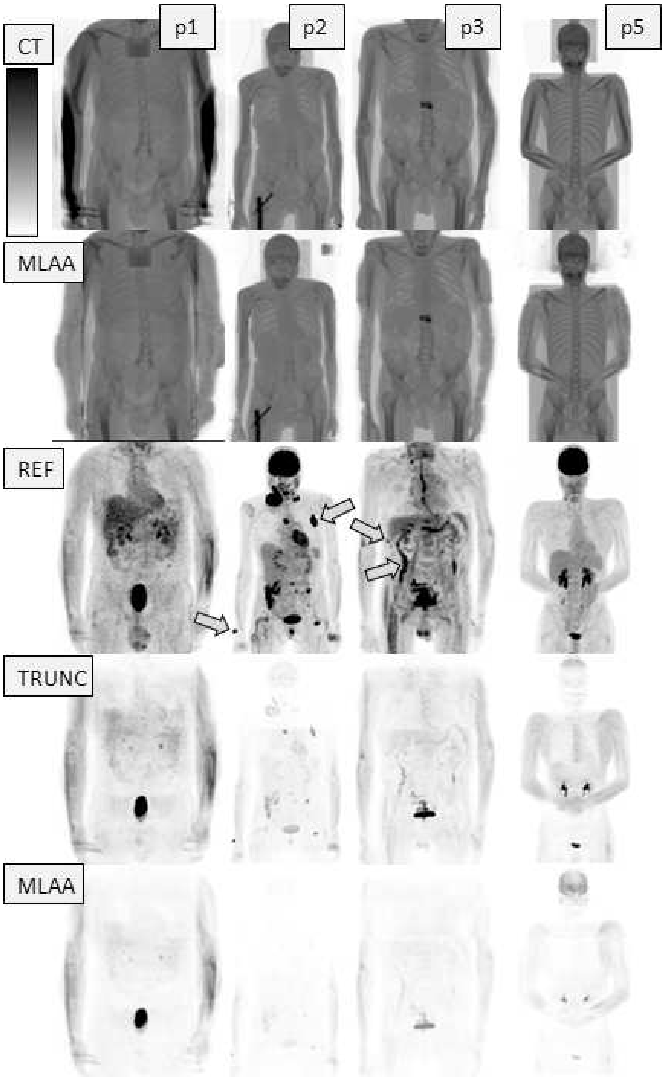

Fig. 6. Maximum intensity projections of the original CT-based attenuation map (row 1), the truncated attenuation map completed by MLAA (row 2), the reference clinical OSEM reconstruction (row 3). The last two rows show the absolute difference from the reference reconstruction, for OSEM with the truncated attenuation map (row4), and for OSEM with the MLAA-completed attenuation map (row 5). For the activity images (rows 3-5), the grey-scale intensities span an SUV-range of 0 to 5. All reconstructions were done with a scatter estimate from the untruncated attenuation map.

the same study as in figure 5. Figure 9 shows the relative errors, using the untruncated segmented attenuation map as the reference. The errors are slightly smaller than when no segmentation was applied (fig. 7).

D. Influence of scatter correction

A result of MLAA-based completion without scatter correction is shown in figure 10 (patient 5). In the absence of scatter correction, the shape of the arms estimated by MLAA was similar, but the estimated attenuation coefficients were slightly lower (5.4%, based on a large VOI containing the right arm) than when scatter was taken into account. This indicates that one can make a first MLAA reconstruction without or with approximate scatter correction. With this first attenuation image an accurate scatter estimate can be computed, which would be used for a final MLAA calculation. Alternatively, the scatter estimation could be included as a part of the iterative MLAA procedure.

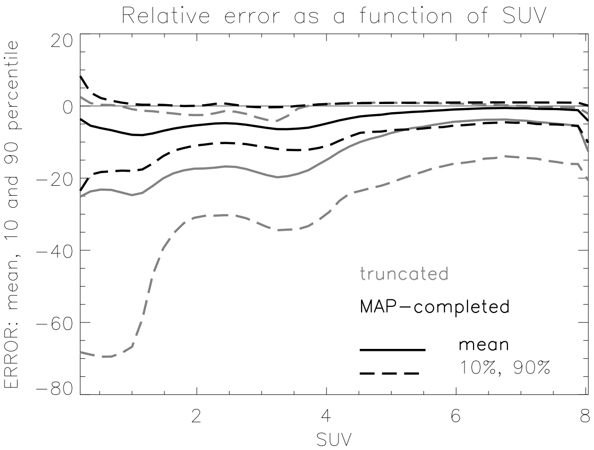

Fig. 7. The relative error in the reconstructed PET images as a function of the reference SUV value. For each SUV value, the mean relative error (solid lines) and the [10%, 90%] confidence interval (dashed lines) are shown. In gray are the errors for the case with truncation, in black for the case of truncation + MLAA-based completion. The reference PET values are taken from the untruncated attenuation image. The curves are computed from all 34×10^6 voxels with SUV > 0.1 from the five patient studies.

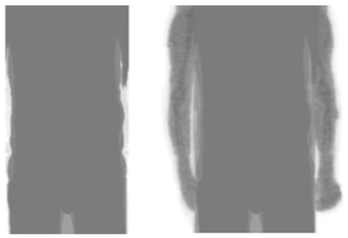

Fig. 8. Maximum intensity projection of the truncated segmented attenuation map (left) and the corresponding image completed with MLAA (right).

The MLAA-based completion is not perfect, and as shown above, it tends to underestimate the attenuation in the arms. Therefore, we verified if the scatter estimated with [25] was affected by these differences. MLAA was applied to complete a truncated attenuation map (using the scatter estimate from the untruncated CT). Then, the MLAA-attenuation map was used to produce a new scatter estimate. Figure 11 compares the scatter profiles from the CT-based attenuation map to those from the truncated and the MLAA-completed ones (patient 4). As expected, truncation changes the scatter profiles significantly. The CT-based and MLAA-based scatter profiles are virtually identical.

E. MLAA-reconstruction of cold objects

Fig 12 shows the setup and results of the experiment to test the ability for reconstructing the six cold rods in front of the patient. The figure shows the true and truncated attenuation images. The rods are not present in the truncated attenuation image. All six rods can be identified in the reconstruction. The reconstruction of the rods is better for the thicker and denser ones. Quantitative comparison is not obvious, because the reconstructed rods are less dense but thicker than the true ones. Attempting to obtain a meaningful number, we computed a forward projection through the rods, producing an image of their linear attenuation contributed to the sinogram.

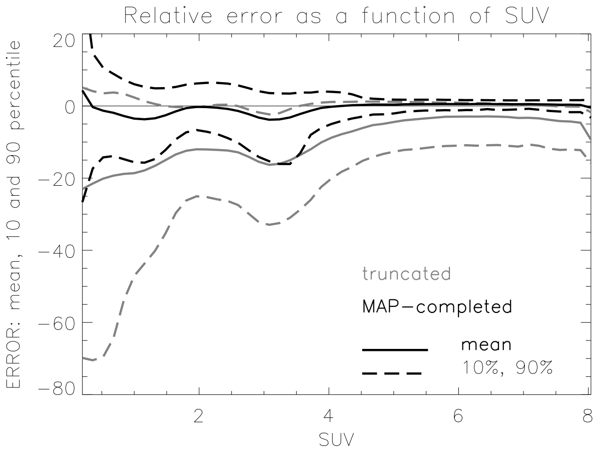

Fig. 9. The relative error in the reconstructed PET images as a function of the reference SUV value for the segmented attenuation maps (compare to fig 7).

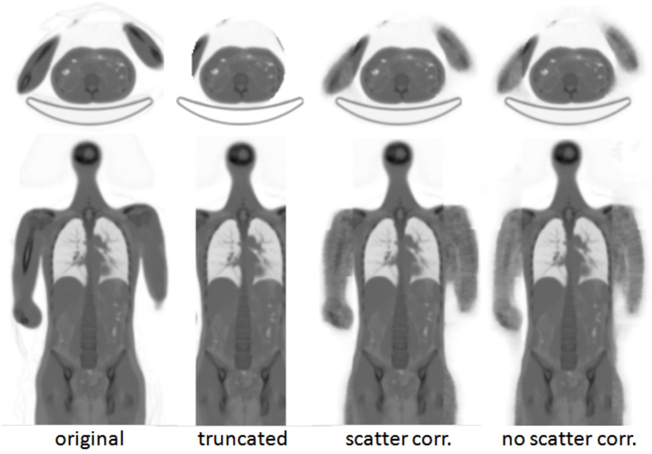

Fig. 10. Transaxial and coronal slices of the original attenuation image, the truncated image, and the MLAA images obtained with and without scatter correction.

Regions defined on the reference image were copied to the image derived from MLAA. The mean values in those regions are compared in Table III (those are dimensionless numbers: i.e. attenuation coefficient times distance). Also the non-zero MLAA attenuation in a region between the rods is reported (backg).

TABLE III
ATTENUATION VALUES FOR THE 6 COLD RODS AND THE BACKGROUND: MLAA VERSUS REFERENCE

	rod1	rod2	rod3	rod4	rod5	rod6	backg
True	0.143	0.106	0.060	0.038	0.032	0.030	0
MLAA	0.132	0.090	0.048	0.024	0.023	0.028	0.011

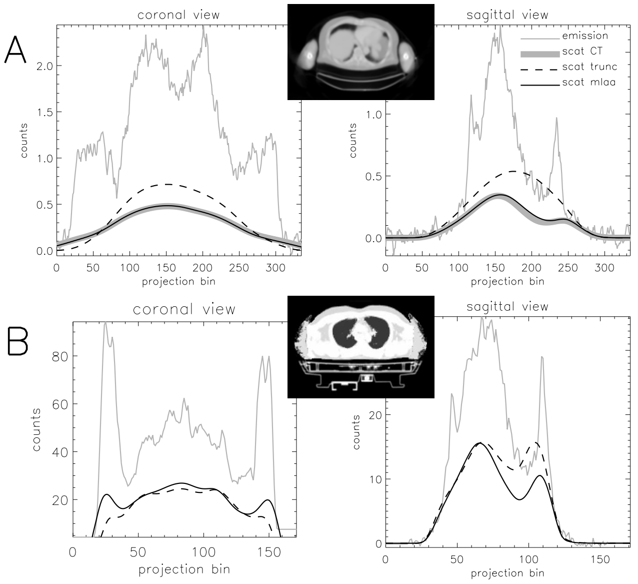

Fig. 11. **Panel A**: coronal and sagittal profiles through the sinogram for a single slice (shown between the plots). The thin gray line is a profile through the emission sinogram (corrected for detector sensitivity but not for attenuation). The other curves are the scatter profiles estimated using the CT-based attenuation (thick gray), the truncated attenuation (dashed black) and the MLAA-completed attenuation (solid black). **Panel B**: same result for the PET/MRI study. In this plot, there is no gold standard (thick gray curve).

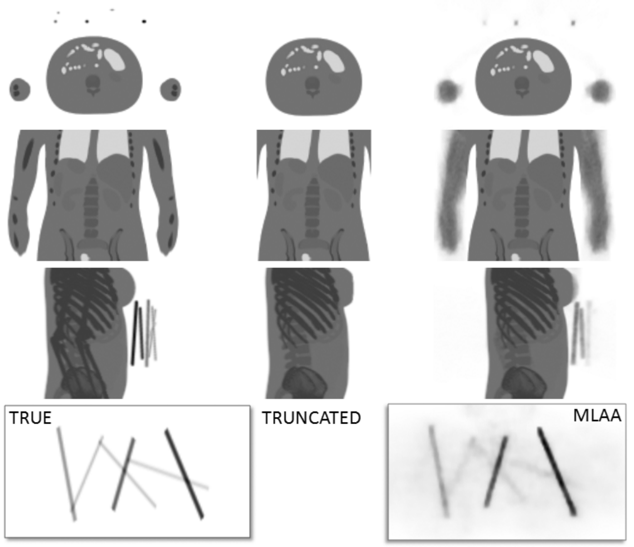

Fig. 12. The left column shows a transaxial slice, a coronal slice and a maximum intensity projection of the true attenuation image; the image at the bottom left is a maximum intensity projection of the six rods located in front of the patient. The central column shows the corresponding images after truncation. This image does not contain the rods. The right column shows the corresponding images after MLAA-completion.

F. First results for a hybrid PET/MRI system

Fig. 13 shows the transaxial and coronal slices through the reconstructed PET image obtained using the truncated and extended attenuation map. As was the case for the truncated CT studies, the uptake values in the arms of the reconstructed emission image seem to be free of artifacts and are probably closer to the true value when the extended attenuation map was used. Scatter profiles were analyzed as well, a result is shown in figure 11, but in this case, no ground truth scatter profile based on untruncated data is available.

V. DISCUSSION

In experiments not shown here, we found that MLAA did not produce good reconstructions of the patient table, but it did reconstruct small metal objects present in the table. MLAA also yielded a useful reconstruction of the cold rods in the

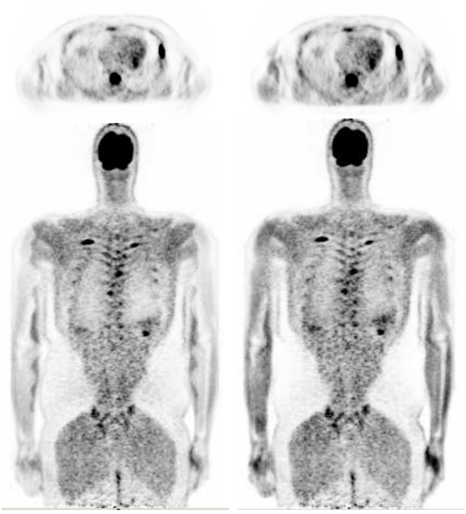

Fig. 13. PET/MR patient scan: transaxial and coronal slices through the PET image, attenuation corrected with the truncated attenuation map (left) and with the MLAA extended attenuation map (right).

NCAT-phantom experiment. We assume that small attenuating objects yield very localised inconsistencies in the sinogram, which are more easily reconstructed than the inconsistencies produced by large smooth objects with low mu-values. It has been reported previously that algorithms such as MLAA suffer from "cross-talk" between the activity and attenuation values: a localised decrease of the activity can be compensated well with a corresponding localised decrease of the attenuation, to yield almost the same sinogram. However, in the cold background, MLAA cannot decrease the activity because of the non-negativity constraint and as a result, the cross-talk effect does not seem to hamper the reconstruction of detailed cold objects in the background.

In our simulation experiments and in the patient study, there was activity in the part of the object that was truncated in the attenuation map. This is typically the case with ^{18}F-FDG, this tracer has a non-negligible uptake almost everywhere in the body. However, for more specific tracers, the activity in the arms can be very low. The performance of MLAA may be poor in such cases, and would probably be worse than the performance for the cold rods. This is because the arms are much larger and their attenuation does not produce such localised sinogram inconsistencies. A possible remedy could be to put a few (stationary) point sources in the field of view, which would supply additional transmission information. As always, these sources will be most effective if a technique is used to separate their contribution from the emission activity [30]. It is straightforward to extend MLAA to use not only an emission scan, but also a (possibly incomplete) transmission scan. Our preliminary simulation experiments indicate that the addition of only a few point sources stabilizes the estimation problem considerably, reducing the dependence on the prior. We have not yet studied the performance and prior parameter selection of MLAA for tracers with low non-specific uptake, future research will be devoted to this issue.

In [10], some artificial operations had to be introduced to ensure that the attenuation of the background was set to zero. Here, this turned out to be unnecessary, because the relative difference prior [22] was used as a regularizer. In a (nearly) zero background, small fluctuations yield large relative differences, and therefore very strong smoothing by the relative difference prior. In contrast, the smoothing effect of the quadratic or Huber priors in the same background would be far less, because the absolute differences between neighbouring voxel values are always fairly small in the background.

As shown in figure 2, a proper selection of the strengths of the priors is essential to obtain good results. The priors have a very small effect on the noise propagation, but they do affect the pixel bias in the final activity image. The selection of β_μ seems to be the more critical one. Fortunately, the minimum is not too sharp, and the minimum bias is fairly close to the reference bias value, obtained with OSEM using the exact attenuation correction. In agreement with this simulation result, we could obtain good results with the same setting of the priors for all five patients studies. This suggests that a fixed set of parameters could be used for a particular scan protocol in clinical routine.

MLAA and similar algorithms suffer from cross-talk between activity and attenuation [10], [13]. With proper constraining, the algorithm performed well for estimating uniform attenuators, but results were poor for non-uniform attenuation in the thorax [10]. Fortunately, for the problem studied here, no lung attenuation must be reconstructed. To counteract cross-talk, the absolute intensity prior P_1 favors soft tissue but not bone, although the truncated region will typically include bone. Adding an additional mode for bone would increase the number of local maxima of the prior and might cause convergence problems. Note, however, that the prior does not exclude the presence of higher attenuation than tissue, and some bone-like structures are actually visible in figures 5, 6 and 10. This successful bone reconstruction may be due to the low activity in the bones, which reduces the freedom for cross-talk, because of the non-negativity constraint.

VI. CONCLUSION

A modification of the previously developed MLAA algorithm has been proposed, to estimate the missing parts in a truncated attenuation map. The method has been validated on a set of PET/CT patient studies with simulated truncation. The experiments also indicate that the method is not sensitive to small segmentation errors in the known portion of the attenuation map. Failure to correct for scatter resulted in a slight underestimation of the attenuation coefficients, but the shape of the truncated arms was well reconstructed. This behaviour is related to the effective μ concept [31]. This suggests that the approach can be combined with image based scatter estimation algorithms. In a simulation experiment, the MLAA algorithm produced useful reconstructions of cold thin rods with medium to low attenuation coefficients. Therefore, the MLAA method seems to be suitable for the completion of MRI-based attenuation maps in hybrid PET/MRI systems. The methodology is applicable to PET/CT systems as well.

VII. APPENDIX

The standard MLEM (or OSEM) algorithm can be written as a gradient ascent algorithm as follows:

$$\hat{\lambda}_j^{n+1} = \hat{\lambda}_j^n + \left(\sum_i g_{ij} \hat{a}_i \frac{y_i - \bar{y}_i}{\bar{y}_i} \right) \Big/ \frac{\sum_i g_{ij} \hat{a}_i}{\hat{\lambda}_j^n} \tag{8}$$

where superscript n indicates the sub-iteration number, the summation over i is restricted to the current subset of projections, and $\bar{y}_i$ is given by (1). The MLTR algorithm [10], [32] can be written as

$$\hat{\mu}_j^{n+1} = \hat{\mu}_j^n - \frac{\partial L}{\partial \mu_j} \Big/ \sum_k \frac{\partial^2 L}{\partial \mu_j \partial \mu_k} \tag{9}$$

where L is the log likelihood function (3). Using the approximation $\bar{y}_i \simeq y_i$ in the denominator this becomes:

$$\hat{\mu}_j^{n+1} = \hat{\mu}_j^n + \frac{\sum_i l_{ij} \frac{\bar{y}_i - s_i}{\bar{y}_i} (\bar{y}_i - y_i)}{\sum_i l_{ij} (\sum_{k \in U} l_{ik}) \frac{(\bar{y}_i - s_i)^2}{\bar{y}_i}}. \tag{10}$$

Because the projection (summation over k) in the denominator can be restricted to the pixels in the unknown part of the attenuation map U, the updates are higher (and convergence is better) when that region is smaller. The relative difference prior can be written as:

$$M(x) = -\frac{1}{2} \sum_j \sum_k w_{jk} \frac{(x_j - x_k)^2}{x_j + x_k + \gamma |x_j - x_k|}. \tag{11}$$

where $w_{jk} = w_{kj}$ defines the weights assigned to differences between neighbouring pixels. We have used $w_{jk} = 1$ for 4 (2D) or 6 (3D) direct neighbors and $w_{jk} = 0$ for all others. As shown in [22], the matrix of second derivatives is negative semi-definite, so it does not add local maxima. In every iteration a truncated Taylor series around the current solution is computed:

$$\begin{aligned} M(x + \Delta x) &\simeq T_1(\Delta x) \qquad (12) \\ &= M(x) + \sum_j \frac{\partial M}{\partial x_j} \Delta x_j + \sum_{j,k} \frac{\partial^2 M}{\partial x_j \partial x_k} \frac{\Delta x_j \Delta x_k}{2} \end{aligned}$$

To compute a surrogate function $T_2(\Delta x)$ for the quadratic approximation $T_1(\Delta x)$, we note that

$$\begin{aligned} &\sum_{j,k} \frac{\partial^2 M}{\partial x_j \partial x_k} \frac{\Delta x_j \Delta x_k}{2} \\ = &\sum_{j,k} w_{jk} \frac{-4x_k^2 \Delta x_j^2 + 4x_j x_k \Delta x_j \Delta x_k}{(x_j + x_k + \gamma |x_j - x_k|)^3} \\ \geq &\sum_{j,k} w_{jk} \frac{-8x_k^2 \Delta x_j^2}{(x_j + x_k + \gamma |x_j - x_k|)^3} \qquad (13) \end{aligned}$$

since $4x_j x_k \Delta x_j \Delta x_k \geq -2x_k^2 \Delta x_j^2 - 2x_j^2 \Delta x_k^2$. Inserting this in (12) yields the surrogate function $T_2(\Delta x)$ such that $M(x) = T_1(0) = T_2(0)$ and $M(x + \Delta x) \simeq T_1(\Delta x) \geq T_2(\Delta x)$. Maximising $T_2(\Delta x)$ is easy because the variables Δx_j are separated, and it is guaranteed to increase $T_1(\Delta x)$. Therefore, if the quadratic approximation holds, it should also increase $M(x + \Delta x)$. Setting the derivatives of T_2 with respect to Δx_j to zero yields

$$\Delta x_j = \frac{\partial M}{\partial x_j} \Big/ \sum_k w_{jk} \frac{16 x_k^2}{(x_j + x_k + \gamma |x_j - x_k|)^3} \tag{14}$$

To further simplify the computations, we assume that the image tends to agree well with the prior, such that $x_k \simeq x_j$. Replacing x_k with x_j in the denominator finally yields

$$\Delta x_j = \frac{\partial M}{\partial x_j} \Big/ \sum_k \frac{2 w_{jk}}{x_j}. \tag{15}$$

In (8) and (10) MLEM and MLTR have been written as gradient ascent algorithms of the form $\Delta x_j = \frac{\partial L}{\partial \Delta x_j} / N_j$. To incorporate the prior in MLEM, we simply add the numerators and denominators of (15) and (8), and similar for MLTR. For MLTR this is natural, because its denominator is also the second derivative of a surrogate function. For MLEM the justification is less obvious, but we obtain good results in practice.

The intensity prior P_1 was implemented as explained in [10] using only two modes: the linear attenuation coefficients of air and tissue. The range of the "air" mode was $[0, \mu_{tissue}/2]$, that of the "tissue" mode $[\mu_{tissue}/2, \infty]$, and the two defining Gaussians had the same standard deviation. Following the recipe of [10], the gradient of P_1 is computed as follows. Let μ_a and μ_T denote the attenuation coefficients of air and tissue, respectively. We also define $b = (\mu_a + \mu_T)/2$. This represents the point of transition between the two modes. Finally, $a = (\mu_a + b)/2$ and $c = (b + \mu_T)/2$. The gradient of the prior P_1 can then be written as:

$$\begin{aligned} \frac{\partial P_1}{\partial \mu_j} &= -\frac{\mu_j - \mu_a}{\sigma^2} \quad \text{if } \mu_j < a \\ &= \frac{\mu_j - b}{\sigma^2} \quad \text{if } a \leq \mu_j < c \\ &= -\frac{\mu_j - \mu_T}{\sigma^2} \quad \text{if } c \leq \mu_j \qquad (16) \end{aligned}$$

Note that this is a piecewise linear function, because the prior is composed of Gaussians, and the gradient of the logarithm of a Gaussian is a linear function.

REFERENCES

[1] P. Kinahan, B. Hasegawa, and T. Beyer, "X-ray-based attenuation correction for positron emission tomography/computed tomography scanners," *Semin Nucl Med*, vol. 33, pp. 166–179, 3 2003.

[2] M. Eiber, A. Martinez-Möller, M. Souvatzoglou, K. Holzapfel, A. Pickhard, D. Lffelbein, I. Santi, E. Rummeny, S. Ziegler, M. Schwaiger, S. Nekolla, and A. Beer, "Value of a Dixon-based MR/PET attenuation correction sequence for the localization and evaluation of PET-positive lesions," *Eur J Nucl Med Mol Imaging*, vol. 38, pp. 1691–1701, February 2011.

[3] M. Hofmann, B. Pichler, B. Schölkopf, and T. Beyer, "Towards quantitative PET/MRI: a review of MR-based attenuation correction techniques," *Eur J Nucl Med Mol Imaging*, vol. 36 (Suppl 1), pp. 93–104, March 2009.

[4] J. Hsieh, E. Chao, J. Thibault, B. Grekowicz, A. Horst, S. McOlash, and T. Myers, "A novel reconstruction algorithm to extend the CT scan field-of-view," *Med Phys*, vol. 31, pp. 2385–2391, 9 2004.

[5] A. Zamyatin and S. Nakanishi, "Extension of the reconstruction field of view and truncation correction using sinogram decomposition," *Med Phys*, vol. 34, pp. 1593–1604, 2007.

[6] S. Manglos, G. Gagne, A. Krol, F. Thomas, and R. Narayanaswamy, "Transmission maximum-likelihood reconstruction with ordered subsets for cone beam CT," *Phys Med Biol*, vol. 40, pp. 1225–1241, 1995.

[7] Y. Censor, D. Gustafson, A. Lent, and H. Tuy, “A new approach to the emission computerized tomography problem: simultaneous calculation of attenuation and activity coefficients,” *IEEE Trans Nucl Sci*, vol. NS-26, pp. 2775–2279, 1979.

[8] F. Natterer, “Determination of tissue attenuation in emission tomography of optically dense media,” *Inverse Problems*, vol. 9, pp. 731–736, 1993.

[9] A. Welch, R. Clack, F. Natterer, and G. Gullberg, “Toward accurate attenuation correction in SPECT without transmission measurements,” *IEEE Trans Med Imaging*, vol. 5, pp. 532–541, 1997.

[10] J. Nuyts, P. Dupont, S. Stroobants, R. Benninck, L. Mortelmans, and P. Suetens, “Simultaneous maximum a-posteriori reconstruction of attenuation and activity distributions from emission sinograms,” *IEEE Trans Med Imaging*, vol. 18, pp. 393–403, May 1999.

[11] A. Bronnikov, “Reconstruction of attenuation map using discrete consistency conditions,” *IEEE Trans Med Imaging*, vol. 19, pp. 451–462, May 2000.

[12] K. H and N. H, “A new approach to SPECT attenuation correction without transmission measurements,” *Nuclear Science Symposium and Medical Imaging Conference*, pp. 13–59 – 13–62, 2000.

[13] A. Krol, J. Bowsher, S. Manglos, D. Feiglin, M. Tornai, and F. D. Thomas, “An EM algorithm for estimating SPECT emission and transmission parameters from emission data only,” *IEEE Trans Med Imaging*, vol. 20, pp. 218–232, March 2001.

[14] V. Panin, G. Zeng, and G. Gullberg, “A method of attenuation map and emission activity reconstruction from emission data,” *IEEE Trans Nucl Sci*, vol. 48, pp. 131–138, 2001.

[15] F. Crepaldi and A. D. Pierro, “Activity and attenuation reconstruction for positron emission tomography using emission data only via maximum likelihood and iterative data refinement,” *IEEE Trans Nucl Sci*, vol. 54, pp. 100–106, 2007.

[16] F. Natterer, *The mathematics of computerized tomography*. SIAM, 2001.

[17] M. Defrise and X. Liu, “A fast rebinning algorithm for 3D positron emission tomography using John’s equation,” *Inverse Problems*, vol. 15, pp. 1047–1065, 1999.

[18] V. Panin, F. Kehren, J. Hamill, and C. Michel, “Application of discrete data consistency conditions for selecting regularization parameters in PET attenuation map reconstruction,” *Phys Med Biol*, vol. 49, pp. 2425–2436, 2004.

[19] C. Laymon and J. Bowsher, “A log likelihood based method for recovery of localized defects in PET attenuation-correction images,” *IEEE Nucl Sci Symp Conf Record*, pp. 2710–2714, October 2004.

[20] A. Salomon, A. Goedicke, B. Schweizer, T. Aach, and V. Schulz, “Simultaneous reconstruction of activity and attenuation for PET/MR,” *IEEE Trans Med Imaging*, vol. 30, p. 3, 804-813 2011.

[21] C. Laymon, J. Bowsher, and T. Turkington, “Recovery of localized defects in PET attenuation-correction images,” *IEEE Nucl Sci Symp Conf Record*, pp. 1949–1952, October 2003.

[22] J. Nuyts, D. Bequé, P. Dupont, and L. Mortelmans, “A concave prior penalizing relative differences for maximum-a-posteriori reconstruction in emission tomography,” *IEEE Trans Nucl Sci*, vol. 49, pp. 56–60, 2002.

[23] B. D. Man, J. Nuyts, P. Dupont, G. Marchal, and P. Suetens, “Reduction of metal streak artifacts in x-ray computed tomography using a transmission maximum a posteriori algorithm,” *IEEE Trans Nucl Sci*, vol. 47, pp. 977–981, March 2000.

[24] R. L. MH Hudson, “Accelerated image reconstruction using ordered subsets of projection data,” *IEEE Trans Med Imaging*, vol. 13, pp. 601–609, 1994.

[25] C. Watson, “New, faster, image-based scatter correction for 3d pet,” *IEEE Trans Nucl Sci*, vol. 47, pp. 1587–1594, 2000.

[26] C. Byrne, *Applied iterative methods*. Wellesley, MA, USA: A K Peters, Ltd, 2008.

[27] C. Laymon, J. Bowsher, J. Carney, and T. Blodgett, “Scatter correction requirements for likelihood-based attenuation artifact correction in PET,” *IEEE Nucl Sci Symp Conf Record*, pp. 2151–2154, 2006.

[28] W. Segars and B. Tsui, “Study of the efficacy of respiratory gating in myocardial SPECT using the new 4-D NCAT phantom,” *IEEE Trans Nucl Sci*, vol. 49, p. 3, 675-679 2002.

[29] V. Panin, “Ordered subsets acceleration of iterative algorithm for variance reduction on compressed sinogram random coincidences,” *IEEE Nucl Sci Symp Conf Record*, pp. 2986–2990, October 2011.

[30] C. Thomson, R. Lecomte, and J. Cadorette, “Feasibility of using beta-gamma coincidence for 3D PET attenuation correction,” *IEEE Trans Nucl Sci*, vol. 47, pp. 1176–1181, 2000.

[31] C. Michel, A. Bol, A. D. Volder, and A. Goffinet, “Online brain attenuation correction in pet: towards a fully automated data handling in a clinical environment,” *Eur J Nucl Med*, vol. 15, pp. 712–718, 1989.

[32] J. Nuyts, B. D. Man, P. Dupont, M. Defrise, P. Suetens, and L. Mortelmans, “Iterative reconstruction for helical ct: a simulation study,” *Phys Med Biol*, vol. 43, pp. 729–737, 1998.